MeCP2 regulates the timing of critical period plasticity that shapes functional connectivity in primary visual cortex

Keerthi Krishnan[a,1], Bor-Shuen Wang[b,1,2], Jiangteng Lu[a], Lang Wang[c], Arianna Maffei[c], Jianhua Cang[b,3], and Z. Josh Huang[a,3]

[a]Department of Neuroscience, Cold Spring Harbor Laboratory, Cold Spring Harbor, NY 11724; [b]Department of Neurobiology, Northwestern University, Evanston, IL 60208; and [c]Program in Neuroscience, Stony Brook University, Stony Brook, NY 11794

Mutations in methyl-CpG-binding protein 2 (*MeCP2*) cause Rett syndrome, an autism spectrum-associated disorder with a host of neurological and sensory symptoms, but the pathogenic mechanisms remain elusive. Neuronal circuits are shaped by experience during critical periods of heightened plasticity. The maturation of cortical GABA inhibitory circuitry, the parvalbumin$^+$ (PV$^+$) fast-spiking interneurons in particular, is a key component that regulates the initiation and termination of the critical period. Using *MeCP2-null* mice, we examined experience-dependent development of neural circuits in the primary visual cortex. The functional maturation of parvalbumin interneurons was accelerated upon vision onset, as indicated by elevated GABA synthetic enzymes, vesicular GABA transporter, perineuronal nets, and enhanced GABA transmission among PV interneurons. These changes correlated with a precocious onset and closure of critical period and deficient binocular visual function in mature animals. Reduction of GAD67 expression rescued the precocious opening of the critical period, suggesting its major role in MECP2-mediated regulation of experience-driven circuit development. Our results identify molecular changes in a defined cortical cell type and link aberrant developmental trajectory to functional deficits in a model of neuropsychiatric disorder.

critical period plasticity | parvalbumin interneurons | visual cortex | Rett syndrome | MeCP2

MECP2 is a methyl-CpG binding protein implicated in the regulation of neuronal chromatin architecture and gene transcription (1–4), especially in response to neural activity and experience during postnatal life (5, 6). Mutations in the *MeCP2* gene cause Rett syndrome (RTT) (7), an autism spectrum disorder. Although MECP2 is broadly expressed in the developing and mature brain (8, 9), patients with RTT achieve expected early postnatal developmental milestones, but later experience a progressive loss of acquired linguistic, social, and motor skills; patients are further characterized by a selected set of postnatal symptoms including stereotyped behaviors and a myriad of sensory and neurological phenotypes (10). *MeCP2* mutations likely impact gene regulation in multiple neuronal (11) and glial cell types (12, 13) and in multiple brain regions; the initial impact may further result in compensatory changes, including maladaptive synaptic plasticity (8, 14), leading to altered developmental trajectory of circuit formation and function. Although numerous mouse models of genetic etiology have been established (15), it has been difficult to identify primary molecular and cellular changes and trace their impact on circuit alterations that underlie behavioral deficits.

Brain circuits are shaped by experience during restricted time windows of early postnatal life. These "critical periods" are crucial for experience-dependent formation of synaptic connections and wiring of functionally related neuronal pathways that underlie sensory, motor, cognitive, social, and language abilities (16). The postnatal maturation of GABA-mediated inhibition

and cortical interneurons is crucial for controlling the timing of critical period plasticity in rodent primary visual cortex (17, 18). There is increasing evidence that dysfunction of GABA signaling is associated with autism disorders and RTT (19–21), raising the possibility that deficits in critical period plasticity may underlie some of the symptoms in these disorders. However, it remains unclear how *MeCP2* mutations impact gene expression in any defined cells and circuits that alter subsequent developmental trajectories, leading to specific functional deficits.

Using a *MeCP2*-null mouse model (22), here we examined experience-dependent development of neural circuits in the primary visual cortex (V1) where the maturation of a defined class of GABA interneurons regulates a critical period of plasticity that shapes visual perception. In V1 of *MeCP2$^{-/y}$* mice, vision onset triggered a significant up-regulation of several key GABAergic markers, including GABA synthetic enzymes GAD67 and GAD65, vesicular GABA transporter, parvalbumin (PV), and components of perineuronal nets (PNNs); several of these are associated with the PV class GABA interneurons. These changes are correlated with an early enhancement of GABA transmission within the PV interneuron network and an accelerated maturation of cortical activity propagation patterns. We further demonstrate

Significance

Rett syndrome is a neurodevelopmental disorder caused by mutations in methyl-CpG-binding protein 2 (*MeCP2*). It is thought to result from altered neuronal connectivity and/or plasticity, possibly through abnormal experience-dependent synapse development, but the underlying mechanisms remain obscure. Using *MeCP2*-null mice, we examined experience-dependent development of neural circuits in the primary visual cortex where GABAergic interneurons regulate a critical period of neural plasticity. We provide evidence that a precocious maturation of parvalbumin$^+$ GABAergic interneurons correlates with the altered timing of the critical period and deficient visual function in the absence of MECP2. Our study begins to establish a link from specific molecular changes in GABAergic neurons to critical period of circuit development and to functional alterations in a mouse model of Rett syndrome.

an early onset and closure of the critical period and deficient visual function: binocular neurons in mature V1 remain mismatched with regard to inputs from the two eyes. Importantly, a reduction of GAD67 level is sufficient to rescue the precocious onset of the critical period, suggesting a significant role for GAD67 in MECP2-mediated regulation of experience-driven V1 circuit development. Together, our studies reveal the impact of *MeCP2* mutation on specific gene expression in identified cell types and developmental stages and trace altered neural circuit wiring to functional deficits.

Results

Accelerated Maturation of Parvalbumin Interneuron Network in V1 of *MeCP2*$^{-/y}$ Mice.

Dani et al. (23) suggested a shift in balance of excitation and inhibition (E/I) in favor of inhibition in mature cortex of *MeCP2*$^{-/y}$ mice, although only subtle changes in GABAergic marker expression were detected in cortical homogenates (21). To determine the impact of *MeCP2* mutation on cortical GABAergic neurons during early postnatal development with cellular and laminar resolution, we examined a panel of GABA markers that directly impact inhibitory transmission. Shortly after eye opening (postnatal day 15, P15), we detected a significant increase in GAD67, the activity-regulated and rate-limiting GABA synthetic enzyme, and the calcium-binding protein parvalbumin, especially in the infragranular layers of *MeCP2*$^{-/y}$ V1 (Fig. 1 A–F). This increased GAD67 expression was more prominent in PV-expressing cells, most of which mature into fast-spiking basket interneurons (24). There was no change in the number of PV interneurons as quantified using a *Rosa26-loxp-STOPloxp-H2BGFP* reporter activated by a *PV-T2A-Cre* allele that labels PV$^+$ nuclei (Fig. S1 A–C), but the level of PV immunofluorescence was increased in a subset of these neurons. These results indicate that more GABAergic neurons express higher levels of GAD67 and PV protein in *MeCP2*$^{-/y}$ V1, compared with WT V1. Increased GAD67 was not only detected in the somata of PV interneurons but also in their presynaptic terminals (or puncta), forming a ring-like structure (Fig. 1 D–F) (18). In addition, immunofluorescence puncta for GAD65 (Fig. 1 G–I), the other GABA synthetic enzyme, specifically localized to presynaptic terminals, and vesicular GABA transporter (VGAT) were also increased (Fig. 1 J–L). Together, these results suggest increased presynaptic vesicles and/or GABA loading, especially in PV interneurons, in *MeCP2*$^{-/y}$ V1.

During the critical period of visual cortical development (25), which spans around 3 wk after eye opening, GABA$^+$ PV interneurons undergo substantial maturation in synaptic innervation and physiological properties, concomitant with increased expression and synaptic localization of GAD67, GAD65, and PV (18, 24, 26). In V1 of *MeCP2*$^{-/y}$ mice, we found that increased expression of GAD67, GAD65, vGAT, and PV persisted to at least the fifth week (Fig. 2 A–I). Interestingly, there was an increase in MECP2 expression in V1 during this period (Fig. S2). Together these results indicate that, upon the onset of visual experience, *MeCP2* deficiency results in a precocious and persistent increase in synaptic localization of molecular machineries for GABA synthesis (GAD67 and GAD65), release (VGAT), and release regulation (PV) in V1, especially in PV interneurons.

Another highly characteristic feature of V1 maturation is the progressive increase of PNNs following eye opening (27). PNNs consist of specialized extracellular matrix proteins such as chondroitin sulfate proteoglycans and interdigitate with synaptic contacts (28). The developmental increase of PNNs is regulated by visual experience (29), and PNNs in mature V1 mainly surround the soma and proximal dendrites of PV interneurons (Fig. 3) (30). Mature PNN is inhibitory for experience-dependent plasticity: its increase in developing V1 correlates with the termination of the critical period and its removal in adult V1 restores plasticity (27, 31, 32). Shortly after eye opening (P15), PNNs in
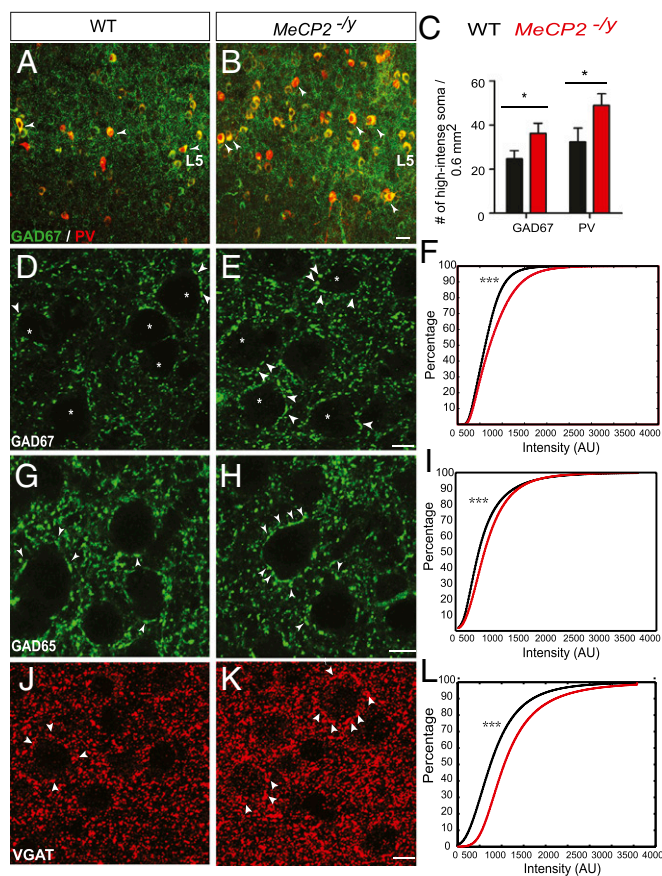

Fig. 1. Increased expression of key components of GABA transmission in *MeCP2*$^{-/y}$ V1 at P15. (A–C) GAD67 (green) and PV (red) expression in the soma of GABAergic neurons in infragranular layers was higher in *MeCP2*$^{-/y}$ compared with WT. Immunofluorescence was carried out without Triton to preserve GAD67 in cell soma. (Scale bar, 50 μm.) Arrowheads point to soma with high GAD67 and PV expression quantified in C (number of high-intense soma/0.6 mm^2). Somata with higher level expression of GAD67 or PV were identified by a threshold method in both genotypes (*Materials and Methods*). (D–L) Increased synaptic localization of GAD67 (D–F), GAD65 (G–I), and VGAT (J–L) in *MeCP2*$^{-/y}$ compared with that in WT. Asterisk indicates somata; arrowheads indicate perisomatic puncta. Note the much more prominent puncta-ring structures surrounding soma in the *MeCP2*$^{-/y}$ panel. Immunofluorescence was carried out with Triton to better reveal synaptic localization of these proteins. (Scale bar, 10 μm.) Cumulative distribution graphs show higher percentage of brighter GAD67 (F), GAD65 (I), and VGAT (L) puncta in *MeCP2*$^{-/y}$ V1 (red) compared with WT (black).

WT V1 were still highly immature: *wisteria floribunda* agglutinin (WFA), which binds the glycosaminoglycan chains of chondroitin sulfate proteoglycans signals, was weak and diffuse, and rather few neurons were surrounded by PNNs (Fig. 3 A and B). In P15 *MeCP2*$^{-/y}$ V1, however, WFA signals were already distinct, and PV cells were surrounded by PNNs especially in infragranular layers (Fig. 3 C and D) (numbers of PNN/0.6 mm^2 in WT were 13.0 ± 3.2 and in *MeCP2*$^{-/y}$: 31.1 ± 4.1, P value = 0.0009). At P30, PNNs in WT V1 began to take on their characteristic appearance, but in relatively small numbers (Fig. 3 E and F), in line with the progression of a normal critical period; in *MeCP2*$^{-/y}$ littermates, however, there were significantly more well-formed PNNs in V1 (Fig. 3 G and H) (numbers of PNN/0.6 mm^2 in WT: 8.8 ± 1.5 and in *MeCP2*$^{-/y}$: 22 ± 3.6, P value = 0.001. Because of significant differences in level and pattern of PNNs at P15 and P30, different threshold criteria were used for defining and quantifying PNN; thus PNN quantifications are not comparable across ages). Taken all together, these results suggest a precocious
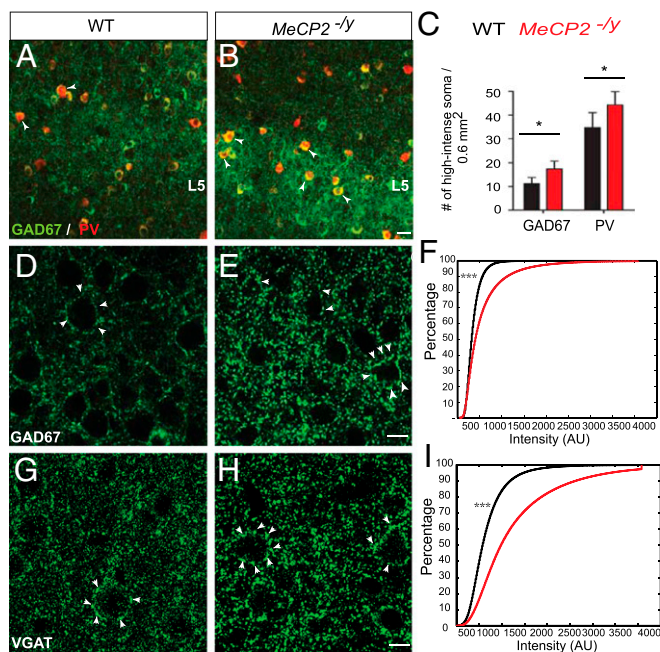
Fig. 2. Increased expression of key components of GABA transmission in $MeCP2^{-/y}$ V1 at P30. (*A–C*) GAD67 (green) and PV (red) expression in the soma of GABAergic neurons in infragranular layers was higher in $MeCP2^{-/y}$ compared with WT. (Scale bar, 50 μm.) Arrowheads point to soma with high GAD67 and PV expression quantified in *C* (number of high-intense soma/0.6 mm²). (*D–L*) Increased synaptic localization of GAD67 (*D–F*) and VGAT (*G–I*) in $MeCP2^{-/y}$ compared with in WT. Arrowheads indicate perisomatic puncta. (Scale bar, 10 μm.) Cumulative distribution graphs show higher percentage of brighter GAD67 (*F*) and VGAT (*I*) in $MeCP2^{-/y}$ V1 (red) compared with WT (black).

maturation of GABAergic interneurons, especially of PV⁺ neurons, after vision onset in $MeCP2^{-/y}$ V1.

Enhancement of GABA Transmission Within the PV Interneuron Network in $MeCP2^{-/y}$ V1. In addition to providing perisomatic inhibition to pyramidal neurons (PyNs), PV cells form extensive connections among themselves through both electrical coupling and reciprocal GABAergic synapses (33, 34). This highly connected network of fast-spiking PV cells plays a key role in the detection of temporal activity patterns within the neocortex (35) and in the generation of network oscillations (34, 36). During postnatal development, substantial maturation of intrinsic and synaptic properties, including GABA transmission among PV cells, converts the PV cell network from a slow to fast signaling device for regulating cortical activity patterns (26, 37). To determine the physiological impact of increased GADs and vGAT levels in PV cells in $MeCP2^{-/y}$ V1, we measured a series of physiological parameters. The intrinsic properties of layer V PV neurons were very similar between WT and $MeCP2^{-/y}$ V1 (Fig. S3). We then measured miniature inhibitory postsynaptic current (mIPSC) in both PV and PyNs in layer V of V1 at P15. Whereas there was no significant change in mIPSC frequency in either cell population (Fig. S4 *C and F*), we found a significant increase in mIPSC amplitude in PV cells (Fig. S4 *A and B*), consistent with increased GAD67 and GAD65 expression in $MeCP2^{-/y}$ V1 interneurons. Interestingly, there was no increase in mIPSC amplitude in PyNs (Fig. S4 *D and E*).

As fast-spiking interneurons, PV cells communicate among each other and transmit inhibitory output to pyramidal neurons typically by firing bursts of action potentials (APs) (34). We therefore performed paired recordings between PV neurons (PV–PV) and PV to PyNs (PV–PyNs) in layer V at P15. Importantly,

when we stimulated PV neurons with a train of action potentials at 20 Hz, we found a significant reduction in synaptic depression in $MeCP2^{-/y}$ V1 compared with that in WT V1 (Fig. 4 *A–C*). This reduction likely results from an enhancement of GABA transmission between PV–PV cells or a change in release probability. This increase in inhibitory transmission dynamics is likely physiologically relevant as PV cells typically fire in the frequency range of 10–40 Hz in vivo (34). On the other hand, there was no such change in inhibitory transmission from PV to PyNs (Fig. 4 *D–F*). An enhancement of GABA transmission among PV cells at P15 would suggest an earlier physiological maturation of these cells which, as a more coherent network, would likely provide more robust inhibitory control over the spatiotemporal flow and processing of neural activity in V1.

Altered Development of Spatiotemporal Activity Propagation in $MeCP2^{-/y}$ V1. From eye opening to the peak of the critical period (fourth postnatal week), there is significant maturation in the spatiotemporal propagation of intracortical activity within rodent V1 (38). Using voltage sensitive dye imaging (VSD), we first confirmed in WT mice, as previously shown in rats, that there is a significant reduction in cortical activation across all layers between P15 and P30 after stimulating the white matter (WM) (Fig. 5) and layer IV (Fig. S5). At P30, the amplitude of peak activation of V1 was significantly reduced, compared with P15, as measured by the time course of VSD signal intensity (Fig. 5 *G–J, Left*) and by the input/output relationship of the VSD signal at increasing stimulation intensities (Fig. 5 *G–J, Right*). In $MeCP2^{-/y}$ V1 at P15, following white matter stimulation, there was a significant reduction in the spatial spread of voltage signaling across all layers compared with those of WT littermates. The observed differences in the peak of the voltage signals was likely due to the reduced amplitude of peak activation in $MeCP2^{-/y}$ V1. The overall patterns of vertical and horizontal propagation of voltage signal were not significantly different between genotypes (Figs. S6 and S7). These data indicate a significant decrease in V1 activation, but no alteration of the direction of propagation over time in $MeCP2^{-/y}$ V1. The spatiotemporal profile of signal propagation in P15 $MeCP2^{-/y}$ mice appeared more similar to that of WT V1 at P30, suggesting an accelerated maturation of the cortical circuit operation. The enhancement of GABA transmission dynamics (39), within PV cell network in particular, in P15 $MeCP2^{-/y}$ V1 likely contributes to the earlier spatial restriction in activity propagation.

A Precocious Critical Period of Plasticity in V1 of $MeCP2^{-/y}$ Mice. Following eye opening, visual experience stimulates the maturation of receptive field properties and guides the functional wiring of V1 circuits during a critical period (25). Importantly, this critical period does not start immediately at vision onset but is initiated more than a week later in rodents (40). Maturation of GABAergic inhibition during this "precritical period" in the third postnatal week is necessary to initiate the critical period, which peaks in the fourth week and closes shortly after (16). A precocious increase of GABA transmission in V1 and precocious maturation of PV cells trigger an earlier onset (18, 41), whereas an accelerated rise of PNNs results in an earlier closure of the critical period (27). We compared the timing of ocular dominance (OD) plasticity in WT and $MeCP2^{-/y}$ mice using a brief monocular deprivation (MD) protocol. As expected, MD in WT mice from P26 induced a significant OD shift (Fig. 6 *A, B,* and *E, Left*), whereas MD from P15 to P20 had no effect (Fig. 6 *A and D, Left*). However, in $MeCP2^{-/y}$ mice, MD from P15 to P20 induced a significant OD shift (Fig. 6 *A and D, Right*) but had no effect at the normal peak of the critical period (i.e., from P26; Fig. 6 *C and E, Right*). Taken together, both the onset and closure of the critical period for OD plasticity were accelerated in $MeCP2^{-/y}$ mice. Furthermore, in ~P30 $MeCP2^{-/y}$ mice, the evoked
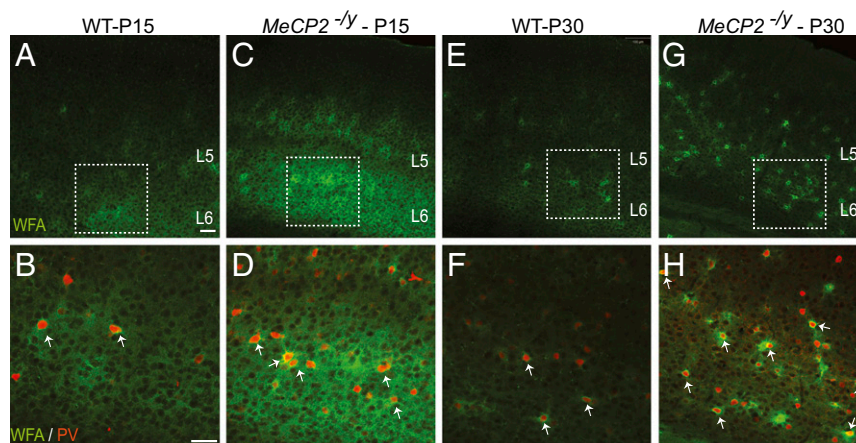
Fig. 3. Precocious maturation of perineuronal nets (PNNs) in *MeCP2*$^{-/y}$ mice. PNNs were identified by lectin WFA (wisteria floribunda agglutinin conjugated to biotin) staining, which labels extracellular matrix components. By P15, weak and diffuse labeling of WFA (green) in WT (*A* and *B*) compared with well-formed PNNs, especially around PV$^+$ neurons (red) in infragranular layers [layers 5 (L5) and 6 (L6) marked at *Top*] of *MeCP2*$^{-/y}$ V1 (*C* and *D*). By P30, WFA staining begins to delineate more well-formed structures in WT V1 (*E* and *F*), whereas PNNs in *MeCP2*$^{-/y}$ V1 are already well-formed and numerous (*G* and *H*). Arrows point to mature nets that encapsulate PV$^+$ neurons. *Lower* panels are higher magnification images of *Top Insets*. (Scale bars, 100 μm for *A*, *C*, *E*, and *G* and 50 μm for *B*, *D*, *F*, and *H*.)

(Fig. S8*A*) and spontaneous (Fig. S8*B*) firing rates in vivo were not significantly different from WT controls, suggesting that the accelerated maturation of PV interneurons did not grossly alter activity levels in *MeCP2*$^{-/y}$ V1.

Binocular Matching of Orientation Preference Is Disrupted in V1 of *MeCP2*$^{-/y}$ Mice. A major function of critical period plasticity is to promote the experience-dependent matching of orientation tuning through the two eyes (42). Shortly after eye opening, V1 neurons exhibit orientation tuning and respond to stimulus to both eyes, but the orientation preference is binocularly mismatched. This initial mismatch is then progressively corrected through visual experience during the critical period, such that individual binocular neurons become tuned to similar orientations through the two eyes (42), a feature presumably important for normal binocular vision. In *MeCP2*$^{-/y}$ mice, monocular orientation tuning profiles of V1 neurons were similar to those in WT mice (Fig. 7 *A–F*), indicating that the basic receptive field properties of V1 neurons are normal in the absence of *MeCP2*. However, the binocular matching of orientation preference failed to occur in *MeCP2*$^{-/y}$ mice (Fig. 7 *A–D* and *G–L*). The degree of matching in ~P30 *MeCP2*$^{-/y}$ mice was significantly worse than age-matched WTs (which had reached the adult level by P30, Fig. 7*L*) and in fact remained at a level preceding the critical period (~P20 WT mice) and similar to that observed after long-term visual deprivation from birth (42). Therefore, the precocious critical period in *MeCP2*$^{-/y}$ mice, which reduces the influence of visual experience on the developing V1, is correlated with and possibly contributes to aberrant wiring of V1 circuits and deficient visual perception.

Rescue of Critical Period Onset by GAD67 Reduction in *MeCP2*$^{-/y}$ Mice. Among the several molecular alterations in V1 of *MeCP2*$^{-/y}$ mice, GAD67 likely has the most significant effect on cellular/vesicular GABA contents and directly impacts the strength of GABA transmission (43). To determine whether the precocious rise in GAD67 expression after eye opening in *MeCP2*$^{-/y}$ mice is a key event in triggering an earlier onset of the critical period, we reduced GAD67 expression by crossing a germ-line *gad1*$^{+/-}$ heterozygous allele into the *MeCP2*$^{-/y}$ background. GAD67 level in P15 *MeCP2*$^{-/y}$; *Gad*$^{+/-}$ V1 was reduced to a level comparable to those in WT V1 (Fig. 8*G*). Importantly, reduction of GAD67 expression in *MeCP2*$^{-/y}$ mice restored PNNs and PV expression

to levels comparable to those in WT V1 (Fig. 8 *A–G*). Furthermore, MD from P15 to P19 induced no OD plasticity in *MeCP2*$^{-/y}$; *Gad*$^{+/-}$ V1, similar to WT mice and in sharp contrast to *MeCP2*$^{-/y}$ (Fig. 8*H*). These results indicate that the accelerated rise of GAD67 expression after vision onset is a key mechanism through which MeCP2 deficiency leads to altered gene expression and a precocious critical period.
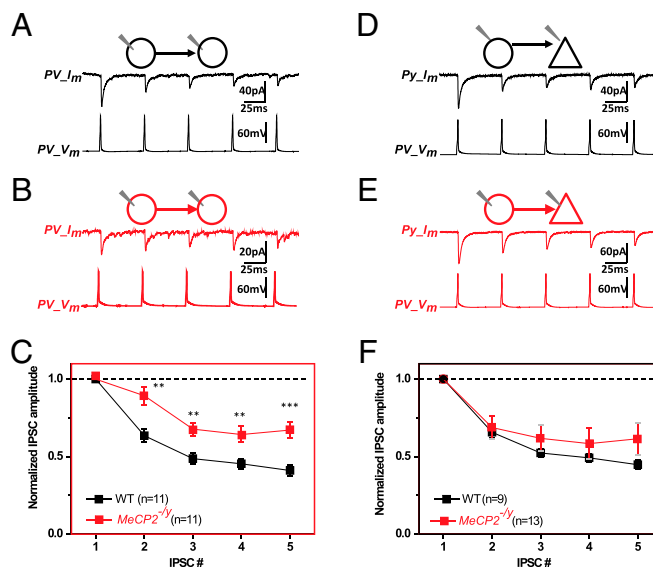

Fig. 4. Enhancement of GABA transmission among PV cells in *MeCP2*$^{-/y}$ V1 at P15. (*A*, *Top*) A schematic of whole-cell patch recording between two PV neurons in layer V of wild-type V1 (black). (*Bottom*) Example IPSCs in a PV neuron (*Upper* trace) evoked by a train of APs (20 Hz) in a presynaptic PV neuron (*Lower* trace), averaged from 20 trials. (*B*) Same recording configuration as in *A* but in PV neurons of *MeCP2*$^{-/y}$ V1 (red). (*C*) Analysis of the short-term dynamics of GABA transmission among PV neurons showed significant reduction in synaptic depression in *MeCP2*$^{-/y}$ V1 (red), compared with WT (black) (*t* test, **$P < 0.01$, and **$P < 0.001$). (*D–F*) Similar analysis of GABA transmission from PV neurons to PyNs in layer V did not show significant changes in short-term synaptic dynamics between WT and *MeCP2*$^{-/y}$.
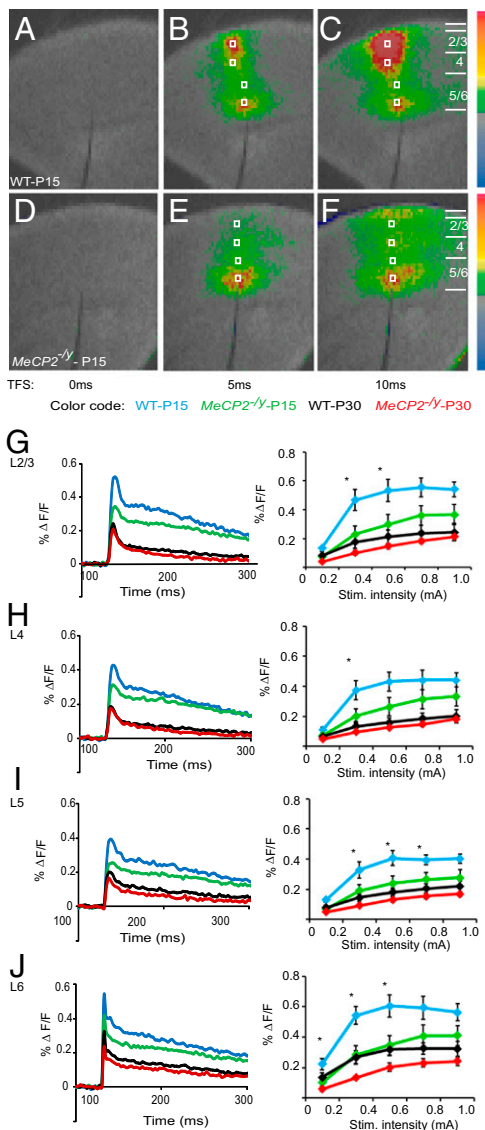
Fig. 5. Accelerated maturation of neural activity propagation through cortical layers after white matter stimulation in *MeCP2⁻/ʸ* V1. Decreased activation of signal through cortical layers in *MeCP2⁻/ʸ* V1 after white matter stimulation, shown with representative sample VSD images for WT (*A–C*) and *MeCP2⁻/ʸ* V1(*D–F*) at 0, 5, and 10 ms. The maximum transition in voltage signal is 1%ΔF/F (deep red color); the minimum is −1%ΔF/F (dark blue). The gray area in the scale bar indicates 0.02%ΔF/F, the detection threshold. White boxes: regions of interest quantified in *G–J, Left*. (*G–J, Left*) Time course of activation in WT L2/3 (*G*), L4 (*H*), L5 (*I*) and L6 (*J*) show significant decrease in amplitude at P30 (black), compared with P15 (76). Voltage signals were measured as the transition in fluorescence from the baseline (ΔF/F). The time course of activation in *MeCP2⁻/ʸ* at P15 (green) across all layers is similar to WT-P30 and significantly reduced compared with WT-P15. (*Right*) Input/output relationship of the VSD signal at increasing stimulation intensities across genotypes and time points suggests precocious maturation in the patterns of cortical activation in *MeCP2⁻/ʸ*. Asterisks indicate statistically significant differences.

Discussion

Although autism spectrum disorders are thought to primarily affect social functioning, there is increasing evidence that unusual sensory processing is at least a concomitant and possibly a cause of many of the behavioral symptoms (44, 45). Here, we use a well-established model of experience-dependent plasticity to discover the impact of MECP2 deficiency in identified cell types and developmental

stages, and trace altered neural circuit plasticity to functional deficits.

It is now well established, largely from studies in rodent primary visual cortex, that the maturation of GABAergic inhibition mediated by a fast-spiking PV interneuron network is a crucial mechanism for triggering the onset and regulating the progression of the critical period for functional wiring in V1 (16, 46). Upon eye opening at ∼P13, visual experience stimulates substantial and progressive activity-dependent maturation of PV cell morphology, connectivity, and physiological properties (18, 24, 43, 47). Visual acuity of *MeCP2⁻/ʸ* mice is comparable to that of WT mice at the time of eye opening, as measured by an optomotor task (21). However, 2–3 d after vision onset (by P15), we found substantial molecular changes (e.g., in GAD67, GAD65, vGAT, PV, and PNN), especially in PV cells, which are indicative of physiological changes. As a rate-limiting GABA synthetic enzyme, GAD67 expression is highly sensitive to input and network activity and directly impacts the magnitude GABAergic transmission (43, 48). Because GAD67 is expressed in all cortical GABAergic neurons and yet appears to manifest cell-type–specific regulation (49), it is crucial to examine activity regulation of GAD67 transcription with laminar and cell-type resolution. A recent study using qRT-PCR on cortical homogenates did not detect changes in GAD67 in adult *MeCP2⁻/ʸ* V1 (21), likely due to the dilution effect by other non-PV interneurons. In our immunohistochemistry study, improved somatic GAD67 staining was achieved by omitting Triton in the protocol to better retain soluble GAD67 in the soma (50). It should be noted that, in addition to mediating cytosolic GABA synthesis, which influences cellular GABA levels, GAD67 and GAD65 form complexes that directly interact with vGAT on synaptic vesicles, thereby facilitating the coupling from GABA synthesis to vesicular packaging (51, 52). The key role of GAD67, GAD65, PV, and vGAT in regulating vesicular GABA content and release (26, 51–53) suggest that alterations in their levels may impact the strength and/or dynamics of GABA transmission (54), especially during fast spiking in PV cells.

In addition to the progressive innervation and inhibitory control of pyramidal neurons, a major aspect of PV cell maturation is the formation of extensive connections among PV cells themselves through both electrical coupling and reciprocal GABAergic synapses (33, 36, 37). The extensive and strong GABA signaling among PV cells is crucial for the formation of a coherent PV network for detecting precise temporal activity patterns (34, 35) and for providing robust and effective inhibitory output in controlling cortical activity patterns (34). Therefore, PV interneurons not only provide certain "levels of inhibition" to PyNs, but also the spatiotemporal pattern of inhibitory control, which is shaped by GABA transmission among PV cells. During the postnatal period in both hippocampus and neocortex, PV interneurons undergo substantial maturation in morphology, connectivity, and intrinsic and synaptic properties (18, 26, 37, 55). A major component of this maturation is the enhancement of GABA signaling among PV cells, which contribute to their conversion from a slow to fast signaling network (37, 55, 56). Importantly, we found a significant reduction in synaptic transmission between PV cells at the 20-Hz range, likely due to a change in release probability, in *MeCP2⁻/ʸ* V1 (Fig. 4 *A–C*). These results are likely physiologically relevant as PV cells are fast spiking and typically fire burst-of-action potentials in the frequency range of 10–40 Hz in vivo (57). Together, these results suggest that, whereas the increase of GAD levels on vesicular GABA content may be quite modest, the concerted increase of several components that impact GABA release machinery (including vGAT and PV) can lead to a selective enhancement of GABA transmission dynamics among PV cells. We suggest that GABA transmission among PV cells in a fast-spiking regime, similar to their
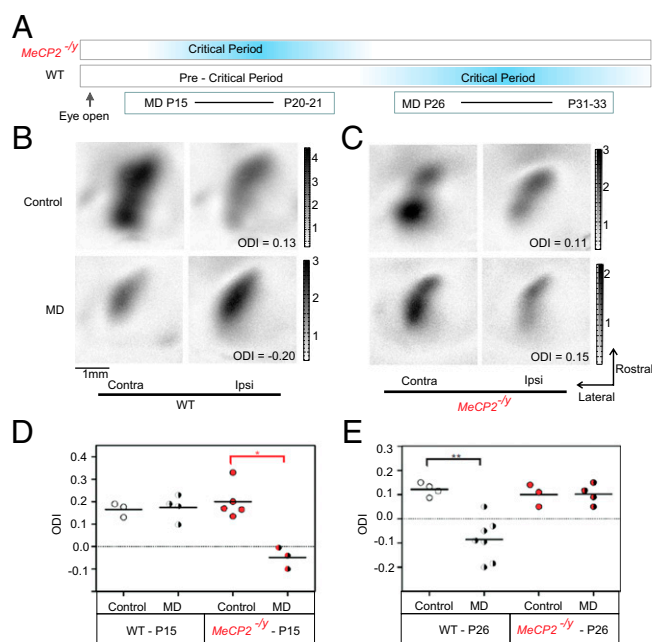
Fig. 6. Precocious critical period in $MeCP2^{-/y}$ mice. (*A*) Schema representing the experimental design for the ocular dominance (OD) plasticity experiments and precocious critical period in $MeCP2^{-/y}$ V1. (*B* and *C*) Representative cortical response magnitude to visual stimuli through the contralateral (Contra) and ipsilateral eye (Ipsi) in control and monocularly deprived WT (*B*) and $MeCP2^{-/y}$ (*C*) V1 during the normal critical period (P26–P32). (*D* and *E*) Quantification of ocular dominance index (ODI). ODI score was calculated as (Contra − Ipsi)/(Contra + Ipsi) for every responsive pixel. (*D*) In WT and $MeCP2^{-/y}$ V1, MD was performed from P15 until intrinsic imaging of OD at P20/21. Whereas WT V1 did not show OD plasticity at this time point (*Left*, white circles), $MeCP2^{-/y}$ V1 displayed significant ODI shift (*Right*, red circles). (*E*) When MD was performed from P26 to P31–P33, WT V1 showed OD plasticity (*Left*), whereas $MeCP2^{-/y}$ V1 did not (77).

physiological operation, is particularly sensitive to levels of molecular machinery for GABA synthesis and release.

Although a simple prediction from an increased GABA transmission among PV cells might be a reduced PV cell firing and thus enhanced network activity, our in vivo recordings at ~P30 did not show alterations in firing rates in $MeCP2^{-/y}$ V1 (Fig. S8). Alternatively, the enhancement of GABA transmission among PV cells at P15 suggests an early maturation of these cells that, together with their electrical coupling and rebound spiking (34), may provide a more coherent inhibitory network in regulating neural activity level and patterns within V1. Indeed, the propagation of neural activity in $MeCP2^{-/y}$ V1 increases in spatial precision compared with that of WT V1 at P15 and resembles that of P30 WT V1 (Fig. 5 and Figs. S5–S7). The accelerated maturation of PV neurons is unlikely due to abnormal sensory input to V1, as the initial synapse formation, elimination, and connectivity between retinal ganglion cells and relay neurons in the lateral geniculate nucleus were similar between WT and $MeCP2^{-/y}$ until the fourth postnatal week (58).

An accelerated maturation of the PV network has been shown to trigger an early onset of the critical period (18, 59). On the other hand, once initiated, critical period plasticity rises, peaks, and terminates with a rather fixed schedule (16), in part defined by several molecular markers including those that mark PNNs (29). Thus, our detection of much enhanced PNN at P15 and P30 further hints at an early closure of the critical period. Our direct measurement of the critical period in $MeCP2^{-/y}$ mice confirmed both these predictions. A recent study using conditional deletion of MeCP2 in PV cells during the third to fourth postnatal week

reported an absence of critical period plasticity (60). This study revealed a cell autonomous role of MeCP2 in PV cell physiology and function. Due to the presence of MECP2 protein in ~85% of PV cells around P20, the onset of critical period plasticity at earlier time points was not measured in these mice (60). In our study, we further demonstrate that the precocious critical period in $MeCP2^{-/y}$ mice, which reduces the influence of visual experience on the developing V1, compromises experience-dependent circuit wiring and visual function: orientation tuning of individual binocular neurons in mature $MeCP2^{-/y}$ V1 remain unmatched between the two eyes. This result is consistent with a recent study that demonstrated the impact of a precocious critical period on binocular vision (61). A previous study reported a deficit in glutamatergic synapse maturation and more protracted OD plasticity in V1 in adult $MeCP2$ heterozygous females (62). As $MeCP2^{+/−}$ female brains consist of a mosaic of MECP2-expressing and MECP2-null cells due to random X-chromosome inactivation, results obtained from these mutant mice are likely not directly comparable with those from $MeCP2^{-/y}$ (null) males. Taken together, our results and previous studies (60, 62) suggest that cell specific, germ-line, and mosaic deletions of $MeCP2$ have different impacts on the developmental trajectory of cortical circuit assembly and function; these should be taken into consideration when discussing their relevance to Rett syndrome.

It is of interest to note that at the retinogeniculate synapse of $MeCP2^{-/y}$ mice, the initial phase of synapse formation proceeds normally (between P9 and P21) but the subsequent experience-dependent phase of synapse remodeling goes awry (58). Given our finding of an early V1 deficit, it is possible that aberrant V1 to LGN influence may contribute to the failure of experience-dependent remodeling of retinogeniculate synapses. Our results
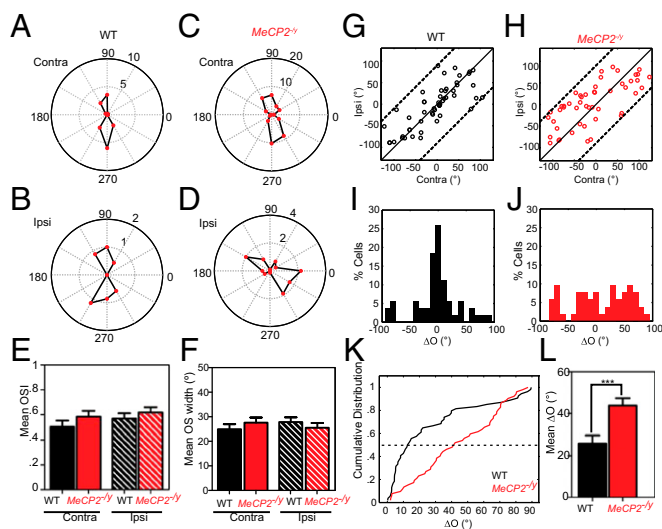

Fig. 7. Deficient binocular matching of orientation tuning in $MeCP2^{-/y}$ V1. (*A–D*) Polar plots of orientation tuning curves of individual binocular neurons in V1. (*A* and *B*) An example WT neuron showing orientation selective responses through the contralateral (Contra, *A*) and ipsilateral (Ipsi, *B*) eye, and matched orientation tuning between the two eyes. (*C* and *D*) An example $MeCP2^{-/y}$ neuron showing sharp orientation tuning monocularly, but mismatch between the two eyes. (*E* and *F*) The mean monocular orientation selectivity index (OSI) (*E*) and orientation selectivity tuning width (OS width) (*F*) were not different between the two genotypes. (*G* and *H*) Correlation of contralateral and ipsilateral orientation preference in WT littermate controls (*G*: 54 cells, 7 mice, P32–P37) and $MeCP2^{-/y}$ mice (*H*: 52 cells, 12 mice, P32–P37). Higher percentage of binocular cells in the WT V1 (*I*) have similar orientation preferences between the two eyes (ΔO), compared with $MeCP2^{-/y}$ (*J*). (*K* and *L*) Cumulative distribution (*K*) and the mean (*L*) of the absolute values of ΔO in WT (black line) and $MeCP2^{-/y}$ (red line).
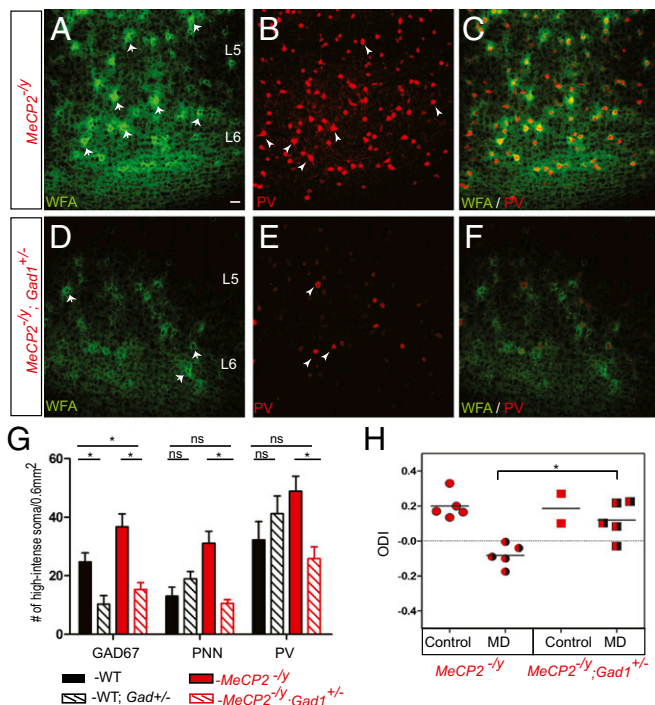
Fig. 8. GAD67 down-regulation rescues precocious onset of critical period in *MeCP2*⁻/ʸ V1. Effects of GAD67 down-regulation on PNN and PV expression in *MeCP2*⁻/ʸ V1. In V1 of compound mutants *MeCP2*⁻/ʸ; *Gad1*⁺/⁻ at P15 (*D–F*), down-regulation of GAD67 reduces the expression of PNN and PV in deeper layers 5 and 6 (L5 and L6) compared with those in *MeCP2*⁻/ʸ V1 (*A–C*). Arrowheads point to cells with high-PV (*B* and *E*) and PNN (*A* and *D*) expression that were quantified in *G*. (*G*) Quantification of the impact of *Gad1* germ-line heterozygote on GAD67, PNN, PV expression in V1 (quantified as high-intensity immunofluorescence soma/0.6 mm²) in WT or *MeCP2*⁻/ʸ background. *Gad1*⁺/⁻ reduces GAD67 levels in *MeCP2*⁻/ʸ mice and restores PNN and PV expression in *MeCP2*⁻/ʸ mice to levels similar to those in WT mice. Asterisks denote statistically significant changes, whereas "ns" denotes no significant change. (*H*) Quantification of ocular dominance index (ODI) in *MeCP2*⁻/ʸ and *MeCP2*⁻/ʸ; *Gad*⁺/⁻ V1 following monocular deprivation from P15 to P20/21. Whereas *MeCP2*⁻/ʸ V1 shows precocious OD plasticity (*Left*, black/red circles), *MeCP2*⁻/ʸ; *Gad*⁺/⁻ V1 no longer exhibits plasticity at this early time point (*Right*, black/red squares).

suggest that *MeCP2* mutations affect basic aspects of visual function, which might impact acquisition of proper social-behavioral abilities. In fact, Djukic et al. (63) reported recently that Rett patients have more difficulty reading emotional expressions than their counterparts and these problems are linked to atypical eye scanning.

Our results suggest that *Gad1* is among the earliest genes misregulated in V1 of germ-line *MeCP2*⁻/ʸ mice, which likely sets in motion a cascade of cellular and circuitry alterations. Importantly, we demonstrate that a reduction of GAD67 expression using *Gad1* heterozygote is sufficient to rescue the expression pattern of multiple GABAergic markers and the early onset of the critical period. This result suggests a causal role of GAD67 in the functional impact of MECP2-mediated gene regulation in experience-driven circuit development. It is possible that the early impact of MECP2 deficiency on GAD67 expression is an up-regulation; this may enhance inhibitory transmission, reduce cortical network activity (23), and promote GABAergic synapse formation (21, 47). On the other hand, because GAD67 transcription is highly sensitive to input activity (48), long-term reduction of activity levels could result in progressive down-regulation and possible silencing of *Gad1* transcription, as a component of circuit-level compensatory changes. Because alterations of GAD67

expression is implicated in numerous neuropsychiatric disorders, understanding the primary cause and subsequent compensatory and maladaptive changes of GAD67 expression in specific cells, circuits, and at defined developmental stages will be critical to elucidate commonly shared circuit level pathogenic mechanisms in these disorders.

GABAergic interneurons are basic components of cortical microcircuits that are conserved across cortical areas. The mechanisms that underlie experience-triggered and MECP2-regulated PV interneuron maturation and critical period timing may also apply to other cortical areas and functional modalities. Hierarchical organization of sensory-motor pathways may develop through a cascade of critical periods as circuit maturation progresses from lower to higher cortical areas (64, 65). Deficient motor, social, and emotional behaviors are characteristic to *MeCP2*⁻/ʸ mice and patients with RTT. Whereas we demonstrate here that MECP2 is necessary to promote experience-dependent alignment of functionally related inputs (e.g., binocular matching onto individual V1 neurons) for proper vision, similar mechanisms may operate in other cortical areas to achieve proper integration of behaviorally relevant sensory-motor inputs or of neuronal pathways that carry appropriate social–emotional information during their corresponding critical periods.

Materials and Methods

All procedures were approved by the Cold Spring Harbor Laboratory and Northwestern University Institutional Animal Care and Use Committee (IACUC) and conducted in the *MeCP2*⁻/ʸ mouse line generated by A. Bird's laboratory (22). PV⁺ neurons were visualized by crossing MeCP2 heterozygotes into the HG (*Rosa26-loxpSTOPloxp-H2BGFP*) line (66). Double mutants for *MeCP2* and *Gad1* were generated by crossing *MeCP2* heterozygote females with *gad1*⁺/⁻ males. All control animals were WT littermates for the mutant mice.

Generation of *gad1*⁺/⁻ Mice. Using homologous recombination in ES cells, a cassette containing destabilized GFP cDNA (D2GFP) was inserted at the translation initiation codon (ATG) of the *Gad1* gene. The goal was to generate a *Gad1* gene transcription reporter allele, but the same allele is also a gene knockout. This design was essentially the same as the widely used *Gad1-GFP* knockin allele (67). Targeted ES clones were identified by PCR and Southern blotting. Positive ES clones were injected into C57BL/6 mice to obtain chimeric mice following standard procedures. Chimeric mice were bred with C57BL/6 mice to obtain germ-line transmission. D2GFP expression was weak and restricted to GABAergic neurons throughout the mouse brain, indicating successful gene targeting. The colony is maintained as heterozygotes because homozygotes are lethal.

Immunostaining. Mice were perfused with saline and 4% (wt/vol) paraformaldehyde at different ages. The brains were removed, postfixed for 18 h in 4% (wt/vol) paraformaldehyde at 4 °C and sectioned at 60-μm thickness using vibratome. Free-floating sections were used for immunostaining using standard protocols. Sections were blocked in 10% (wt/vol) normal goat serum and 1% Triton for 2–3 h, and then incubated overnight with the following primary antibodies: GAD67 (mouse monoclonal; 1:800, Millipore), PV (mouse monoclonal; 1:1,000, Sigma), PV (rabbit polyclonal; 1:1,000, Calbiochem), GAD65 (mouse monoclonal; 1:400, Millipore), VGAT (guinea pig; 1:500, Synaptic Systems), MeCP2 (rabbit; 1:1,000, Cell Signaling), and WFA (1:500; Sigma). Sections were then incubated with appropriate Alexa Fluor dye-conjugated secondary antibodies (1:500; Molecular Probes) and mounted in Fluoromount-G (Southern Biotech). For GAD67 staining, the above mentioned protocol was used for detecting synaptic signal. To obtain GAD67 staining in soma (68), three modifications were made: (*i*) no Triton or detergent was used in the blocking solution or the primary antibody diluent; (*ii*) sections were treated with 1% sodium borohydride to reduce background; and (*iii*) sections were left in primary antibody for 48–60 h at room temperature. Brains were processed blind to the genotype and together at all steps in the process (perfusions, sectioning, immunostaining, and imaging) to minimize variability.

Image Acquisition and Analysis. Visual cortices from at least three animals were used for each developmental stage and genotype. At least four sagittal sections containing the visual cortex from each animal were analyzed. Images

were acquired using the Zeiss LSM510 confocal microscope and analyzed using the LSM Image Browser. To analyze GAD67$^+$, PV$^+$ soma, and PNNs, nonoverlapping Z-stack images (2.5-μm optical sections for 25 μm) were acquired in infragranular layers with a 20× objective (scan zoom of 0.7, area of 0.6 mm^2 per image). Scans from each channel were collected in the "multiple tracks" mode and subsequently merged. Maximum intensity projections of the Z stacks were obtained using the "projection" setting in the Zeiss LSM Image Browser. To count high-intensity soma and mature PNNs, the "contrast" setting in the browser was set to 100 to threshold weaker signals. GAD67$^+$ and/or PV$^+$ somata and mature PNNs were manually counted. Data were represented as mean ± SEM.

To analyze GAD67, GAD65, and VGAT puncta, we focused on perisomatic synapses (18) in layer V of V1. Nonoverlapping Z-stack images (1-μm optical section for 10 μm) were acquired using the 63× oil immersion objective (scan zoom of 1, area of 125 μm^2). Intensity and frequency for representative single optical sections at the same Z position for each image were obtained using the "histogram" function in the browser. Differences between different groups were tested for significance using the Kolmogorov–Smirnov test (KS test). Statistical analyses and graphs were done with Prism (GraphPad Software) and Matlab (Mathworks). As the expression levels of these markers increase during development, settings appropriate for each ages were selected for quantification; thus quantifications are not comparable across ages.

Slice Physiology. Visual cortical slices (300 μm) were prepared from P15–P16 mice. All animals were anesthetized with isofluorane before decapitation. The brain was rapidly dissected and transferred into ice-cold oxygenated artificial cerebrospinal fluid (section ACSF; composition in millimoles: 110 choline-Cl, 2.5 KCl, 4 MgSO$_4$, 1 CaCl$_2$, 1.25 NaH$_2$PO$_4$, 26 NaHCO$_3$, 11 D-glucose, 10 Na-ascorbate, 3.1 Na-pyruvate, pH 7.35, ~300 mOsm) for 1 min. Coronal slices were dissected with a vibratome (HM 650 V, Microm) at 1–2 °C and further incubated with oxygenated ACSF (working ACSF; composition in millimoles: 124 NaCl, 2.5 KCl, 2 MgSO$_4$, 2 CaCl$_2$, 1.25 NaH$_2$PO$_4$, 26 NaHCO$_3$, 11 D-glucose, pH 7.35, ~300 mOsm) at 34 °C for 30 min, and then transferred to ACSF at room temperature (25 °C) for >30 min before use. The recordings were located to the V1 area, using the shape of the hippocampus as the primary landmark.

Whole-cell patch recordings were made with pipettes pulled from borosilicate glass capillaries with filament (1.2 mm outer diameter, 0.69 mm inner diameter; Warner Instruments) with a resistance of 3–6 MΩ. For paired recordings and intrinsic properties experiments, pipettes were filled with a solution containing (in millimoles) 130 potassium gluconate, 15 KCl, 10 sodium phosphocreatine, 10 Hepes, 4 ATP-Mg, 0.3 GTP and 0.3 EGTA, pH 7.3 adjusted with KOH, ~300 mOsm. Layer 5 (L5) PV cells were identified by fluorescence (PV-T2A-cre; HG mice) and PyNs by the giant typical triangular soma and apical dendrites using an upright microscope (BX51; Olympus) equipped with infrared-differential interference contrast (IR-DIC) optics and fluorescence excitation source (X-cite; EXFO). Both IR-DIC images and fluorescence images were captured with a digital camera (Microfire; Optronics). The recordings were performed at 33–34 °C in the chamber perfused with oxygenated working ACSF. Synaptic responses were evoked by presynaptic APs through soma-injected current squares (1.5 ms, 1–1.8 nA). All values were presented as mean ± SEM. Differences between groups were tested for significance using a t test. Statistical analyses and graphs were done with Prism (GraphPad Software) and Matlab (Mathworks). In Fig. 4C and Figs. S3C and S4B, *P < 0.05, **P < 0.01, and ***P < 0.001.

For mIPSC recordings, pipettes were filled with a solution containing (in millimoles) 145 CsCl, 4 NaCl, 0.5 CaCl$_2$, 5 Hepes, 2 ATP-Mg, and 5 EGTA, pH 7.3 adjusted with KOH, ~296 mOsm. For mEPSC recordings, the pipettes were filled with internal solution containing (in millimoles): 20 KCl, 100 K-gluconate, 10 Hepes, 0.2% biocytin, 4 Mg-ATP, 0.3 Na-GTP, and 10 Na$_2$-phosphocreatinine. Layer 5 PV interneurons were identified by fluorescence (PV-T2A-cre; HG mice) and pyramidal neurons by the typical large triangular soma and apical dendrites using an upright microscope (BX51; Olympus) equipped with IR-DIC optics and fluorescence excitation source (X-cite; EXFO). Both IR-DIC images and fluorescence images were captured with a digital camera (Microfire; Optronics). mIPSC recordings were performed at room temperature (23–25 °C) in the chamber perfused with oxygenated working ACSF, which contained 1 μM TTX, 100 μM APV and 20 μM CNOX; voltage clamping at −75 mV without junction potential correction. mIPSC analysis was performed with a total of 14 WT and 12 MeCP2$^{-/y}$ PV cells and 17 WT and 16 MeCP2$^{-/y}$ pyramidal cells. mIPSC data were imported to miniAnalysis for frequency and amplitude inspection. All chemicals were purchased from Sigma-Aldrich and Tocris.

VSD Imaging. VSD imaging was performed as previously described (38, 69). Briefly, Di-4-ANEPPS (Invitrogen; absorption: 496 nm; emission: 705 nm) was dissolved in a 2:1 mixture of ethanol and 10% Chremophor-EL solution (vol/vol in ddH$_2$O; Sigma) and stored as stock solution with the final concentration of 3.3 mg/mL. For staining, a small volume of the stock solution was dissolved in a 1:1 mixture of FBS (Sigma) and oxygenated ACSF to a final Di-4-ANEPPS concentration of 0.2 mM. Before recording, a slice attached to an Omnipore membrane filter was covered with 100 μL staining solution and incubated for 40 min at room temperature in a recovery chamber containing oxygenated ACSF. The slice was then transferred to the recording chamber mounted on an upright microscope (Olympus; BX51WI) and the excess dye was allowed to be washed off for 10 min with constant flow of oxygenated ACSF at 32 °C. During recording, slices were illuminated with a halogen lamp (150W, TH 4–100; Olympus) controlled by a fast-speed electronic shutter (Smart Shutter with Lamda 10B controller; Sutter Instruments). The slice was activated using an extracellular unipolar stimulating electrode covered by a glass pipette (0.1 MΩ; Harvard Apparatus) and placed either in the white matter immediately below the primary visual cortex or in the center of layer IV depending on the experiment. To activate the slice, 0.2-ms pulses were delivered at a series of intensities increased by steps (0.1–0.9 mA).

The fluorescence signal emitted from the slice was recorded by activating the voltage-sensitive dye with light passing through an excitation filter (λ 530 nm) and projecting onto a dichroic mirror (λ 565 nm). The fluorescence generated by the tissue was passed through an absorption filter (λ 595 nm) and collected by a CCD camera (MiCAM02, SciMedia; Brainvision). The shutter controller, the optical signal acquisition, and the stimulus isolation unit (Warner Instruments) were synchronized by an input/output interface (MiCAM 02, SciMedia; Brainvision). A peristaltic pump (Watson-Marlow Sci 400) and a temperature controller (Warner Instruments) were used to maintain the stability of ACSF flow and temperature through the recording.

After the interested area was visually identified, images were collected with a 4× objective with high numerical aperture (NA 0.28; Olympus) and further widening the imaged field with a 0.5× lens placed on the c-mount of the CCD camera. The image resolution was set to 60 × 88 active pixels with single pixel size of 20 μm, allowing to image changes in fluorescence over an area of 1.2 mm × 1.8 mm. The response to each stimulus was recorded, collecting 256 frames at 400 Hz (one image every 2.5 ms) for a total of 640 ms. To obtain a good signal-to-noise ratio, each image sequence resulted from the average of 16 trials recorded every 15 s. The initial light intensity was set to 50% of maximum illumination to allow for the measurement of increases in activity (quantified as decreases in fluorescence and presented as green to red colors in the figure) and possible decreases in activity (quantified as increases in fluorescence and presented as light blue to dark blue in the figure). The transition in fluorescence was normalized to the baseline fluorescence signal collected 50 ms before the stimulation and quantified, and %ΔF/F for each slice was calculated to compare between different conditions. The di-4-ANEPPS has a sensitivity of 10% ΔF/F changes per 100-mV transitions.

Image sequences were analyzed using Brainvision analysis software and ImageJ. Recordings were performed and analyzed blind to the genotype. Data were grouped and compared statistically after the genotype of the animal was revealed. The number of slices and animals for each group was as follows: P15 WT, 6 slices from three animals; P15 MeCP2$^{-/y}$, 8 slices from four animals; P30–P35 WT, 11 slices from three animals; and P30–P35 MeCP2$^{-/y}$, 8 slices from two animals. Data were presented as mean ± SEM. Statistical analysis was performed using SigmaPlot (Systat Software). To determine significance, the Kruskal–Wallis one-way ANOVA on ranks was performed, and if significant, was followed by Dunn's test. P values <0.05 were considered significant.

In Vivo Physiology. WT (n = 7) and MeCP2$^{-/y}$ (n = 12) mice at ages between P32 and P37 were first sedated with an i.p. injection of chlorprothixene (5 mg/kg) and then anesthetized using urethane (0.5–1.0 g/kg in 10% saline solution, i.p.) as described previously (70). Atropine (0.3 mg/kg) and dexamethasone (2.0 mg/kg) were injected s.c. Additional urethane (0.2–0.3 g/kg) was administered as needed. The eyes of the animal were covered by silicon oil to avoid drying. The animal was placed in a stereotaxic apparatus on a heating pad. The animal's temperature was monitored with a rectal thermo probe and maintained at 37 °C through a feedback heater control module (Frederick Haer and Company, FHC). Electrocardiograph leads were attached across the skin to monitor the heart rate continuously throughout the experiment. All experimental procedures were approved by Northwestern University Institutional Animal Care and Use Committee.

A small craniotomy (~2 mm^2) was performed at the left hemisphere to expose the cortex for recording. A total of 5–10 MΩ tungsten microelectrodes

(FHC) were penetrated perpendicular to the pial surface in the binocular zone of V1 (2.8–3.3 mm lateral from the midline and 0.5–0.8 mm anterior from the lambda suture). In each animal, two to six penetrations were made with minimum spacing of 50 µm and cells recorded across all layers were included in our analysis. Electrical signals, both spikes (filtered between 0.3 and 5 kHz and sampled at 25 kHz) and field potentials (filtered between 10 and 300 Hz and sampled at 800 Hz), were acquired using a System 3 Workstation (Tucker-Davis Technologies) and the spike waveforms were further sorted offline into single units using OpenSorter (Tucker-Davis Technologies). The animals were overdosed with Euthasol (150 mg/kg pentobarbital; Virbac) at the end of recording.

Visual Stimuli and Data Analysis. Visual stimuli and analysis followed our previous study. Briefly, visual stimuli were generated with Matlab programs (70) using the Psychophysics Toolbox extensions (71, 72). A CRT video monitor (40 × 30 cm, 60 Hz refresh rate, ~35 cd/m^2 mean luminance) was placed at 25 cm in front of the animal, with its midline aligned with the animal. The stimulus was delivered through either eye separately; i.e., the stimulus was delivered through the eye contralateral to the recorded hemisphere while the ipsilateral eye was occluded, and vice versa.

Drifting sinusoidal gratings were used to determine V1 neurons' orientation selectivity (42). The drifting direction (θ) and spatial frequency of the gratings (full contrast and temporal frequency of 2 Hz) were varied between 0° and 360° (12 steps at 30° spacing), and 0.01–0.08 cycle/degree (four logarithmic steps) in a pseudorandom order. The response to a particular stimulus condition, R, was obtained by averaging the number of spikes over the 1.5-s stimulus duration, across all trials and subtracting the spontaneous rate. The preferred direction was determined as the one that gave maximum response (R_{pref}), averaging across all spatial frequencies. The preferred spatial frequency (pref_SF) was the one that gave peak response at this direction. Responses across all directions at the preferred spatial frequency, R(θ), were used to calculate the preferred orientation, orientation selectivity index (OSI), and tuning width. The maximum R of the 48 conditions was used for evoked neuronal activity, and the average response to blank condition was used for spontaneous neuronal activity.

Half of the complex phase of $\sum R(\theta)*e^{2i*\theta}/\sum R(\theta)$ was calculated (70), which is essentially a weighted mean of θ across a 180° cycle. This value was further converted to the preferred orientation (pref_O) by subtracting 90° because θ was expressed in stimulus direction. The difference in preferred orientation between the two eyes was calculated by subtracting ipsilateral pref_O from contralateral pref_O along the 180° cycle (–90° to 90°). The absolute values of these differences (ΔO) were used in all quantifications (WT: $n = 52$; MeCP2$^{-/y}$: $n = 54$).

OSI was calculated as the ratio of ($R'_{pref} - R_{orth})/(R'_{pref} + R_{orth}$), where R'_{pref} was the mean response of R_{pref} at θ_{pref} and $\theta_{pref+\pi}$ as the two angles have the same orientation, and R_{orth} was the mean response of the two directions orthogonal to the preferred direction. Orientation tuning width was determined by obtaining the half-width at half-maximum response after fitting the tuning curve as the sum of two Gaussians (42, 70). Note that only cells that were well fitted were included in the analysis of tuning width (WT: $n = 32$; MeCP2$^{-/y}$: $n = 33$). All values were presented as mean ± SEM. Differences between groups were tested for significance using the KS test. Statistical analyses and graphs were done with Prism (GraphPad Software) and Matlab (Mathworks). In Fig. 7, ***$P < 0.001$.

Optical Imaging of Ocular Dominance Plasticity. Monocular deprivation of the right eye was performed in WT and MeCP2$^{-/y}$ mice at P15 or P26 under isofluorane anesthesia (1.5–2% in O$_2$) following published procedures (73, 74). Mice whose eyelids were not completely sealed close or those with any indication of corneal damage or cataracts were excluded from the study before imaging. The ocular dominance of these mice was determined 5–7 d later by optical imaging of intrinsic signal (73, 75) under isofluorane anesthesia (0.5–1.5% in O$_2$). A craniotomy was performed to expose the left visual cortex, and the cortex was then covered with agarose and coverslip to form an imaging window. The visual stimulus was a thin bar (2° in height and 20° in width) drifting continuously and periodically upward or downward. It was shown between –5° to 15° azimuth (the vertical meridian defined as 0° with negative values for ipsilateral visual field) and full-screen elevations. The spatial frequency of the drifting bar was one cycle/100°, and temporal frequency one cycle/8 s. Optical images were acquired at 610 nm using a 1M30 CCD camera (Dalsa) and the Fourier component of the reflectance changes was extracted at the temporal frequency of the stimulus as described previously (75).

The response magnitude map evoked by ipsilateral eye stimulation was first smoothed by a uniform kernel of 5 × 5 filter and then thresholded at 30% of the peak response amplitude, to determine the binocular zone for ocular dominance analysis. The ocular dominance index was calculated as the mean of (C – I)/(C + I) of all pixels within the selected region, where C and I represent the response magnitude to the contralateral and ipsilateral eyes, respectively (73). The ODI ranges from +1 to –1, where a positive value indicates a contralateral bias and negative ODI, an ipsilateral bias. The Mann–Whitney test was used to test for statistical significance between two groups in optical imaging experiments. Statistical analyses and graphs were done with Prism (GraphPad Software). In Figs. 6 and 8, *$P < 0.05$ and **$P < 0.01$.

1. Lewis JD, et al. (1992) Purification, sequence, and cellular localization of a novel chromosomal protein that binds to methylated DNA. *Cell* 69(6):905–914.
2. Skene PJ, et al. (2010) Neuronal MeCP2 is expressed at near histone-octamer levels and globally alters the chromatin state. *Mol Cell* 37(4):457–468.
3. Baker SA, et al. (2013) An AT-hook domain in MeCP2 determines the clinical course of Rett syndrome and related disorders. *Cell* 152(5):984–996.
4. Lyst MJ, et al. (2013) Rett syndrome mutations abolish the interaction of MeCP2 with the NCoR/SMRT co-repressor. *Nat Neurosci* 16(7):898–902.
5. Zhou Z, et al. (2006) Brain-specific phosphorylation of MeCP2 regulates activity-dependent Bdnf transcription, dendritic growth, and spine maturation. *Neuron* 52(2):255–269.
6. Ebert DH, et al. (2013) Activity-dependent phosphorylation of MeCP2 threonine 308 regulates interaction with NCoR. *Nature* 499(7458):341–345.
7. Amir RE, et al. (1999) Rett syndrome is caused by mutations in X-linked MECP2, encoding methyl-CpG-binding protein 2. *Nat Genet* 23(2):185–188.
8. Zoghbi HY (2003) Postnatal neurodevelopmental disorders: Meeting at the synapse? *Science* 302(5646):826–830.
9. Kishi N, Macklis JD (2004) MECP2 is progressively expressed in post-migratory neurons and is involved in neuronal maturation rather than cell fate decisions. *Mol Cell Neurosci* 27(3):306–321.
10. Chahrour M, Zoghbi HY (2007) The story of Rett syndrome: From clinic to neurobiology. *Neuron* 56(3):422–437.
11. Chen RZ, Akbarian S, Tudor M, Jaenisch R (2001) Deficiency of methyl-CpG binding protein-2 in CNS neurons results in a Rett-like phenotype in mice. *Nat Genet* 27(3):327–331.
12. Derecki NC, et al. (2012) Wild-type microglia arrest pathology in a mouse model of Rett syndrome. *Nature* 484(7392):105–109.
13. Lioy DT, et al. (2011) A role for glia in the progression of Rett's syndrome. *Nature* 475(7357):497–500.
14. Ramocki MB, Zoghbi HY (2008) Failure of neuronal homeostasis results in common neuropsychiatric phenotypes. *Nature* 455(7215):912–918.
15. Calfa G, Percy AK, Pozzo-Miller L (2011) Experimental models of Rett syndrome based on Mecp2 dysfunction. *Exp Biol Med (Maywood)* 236(1):3–19.
16. Hensch TK (2005) Critical period plasticity in local cortical circuits. *Nat Rev Neurosci* 6(11):877–888.
17. Hensch TK, et al. (1998) Comparison of plasticity in vivo and in vitro in the developing visual cortex of normal and protein kinase A RIbeta-deficient mice. *J Neurosci* 18(6):2108–2117.
18. Huang ZJ, et al. (1999) BDNF regulates the maturation of inhibition and the critical period of plasticity in mouse visual cortex. *Cell* 98(6):739–755.
19. Han S, et al. (2012) Autistic-like behaviour in Scn1a+/- mice and rescue by enhanced GABA-mediated neurotransmission. *Nature* 489(7416):385–390.
20. Chao HT, et al. (2010) Dysfunction in GABA signalling mediates autism-like stereotypies and Rett syndrome phenotypes. *Nature* 468(7321):263–269.
21. Durand S, et al. (2012) NMDA receptor regulation prevents regression of visual cortical function in the absence of Mecp2. *Neuron* 76(6):1078–1090.
22. Guy J, Hendrich B, Holmes M, Martin JE, Bird A (2001) A mouse Mecp2-null mutation causes neurological symptoms that mimic Rett syndrome. *Nat Genet* 27(3):322–326.
23. Dani VS, et al. (2005) Reduced cortical activity due to a shift in the balance between excitation and inhibition in a mouse model of Rett syndrome. *Proc Natl Acad Sci USA* 102(35):12560–12565.
24. Chattopadhyaya B, et al. (2004) Experience and activity-dependent maturation of perisomatic GABAergic innervation in primary visual cortex during a postnatal critical period. *J Neurosci* 24(43):9598–9611.
25. Gordon JA, Stryker MP (1996) Experience-dependent plasticity of binocular responses in the primary visual cortex of the mouse. *J Neurosci* 16(10):3274–3286.
26. Lazarus MS, Huang ZJ (2011) Distinct maturation profiles of perisomatic and dendritic targeting GABAergic interneurons in the mouse primary visual cortex during the critical period of ocular dominance plasticity. *J Neurophysiol* 106(2):775–787.

27. Pizzorusso T, et al. (2002) Reactivation of ocular dominance plasticity in the adult visual cortex. *Science* 298(5596):1248–1251.

28. Miyata S, et al. (2012) Persistent cortical plasticity by upregulation of chondroitin 6-sulfation. *Nat Neurosci* 15(3):414–422, S1-2.

29. Nowicka D, Soulsby S, Skangiel-Kramska J, Glazewski S (2009) Parvalbumin-containing neurons, perineuronal nets and experience-dependent plasticity in murine barrel cortex. *Eur J Neurosci* 30(11):2053–2063.

30. Celio MR (1993) Perineuronal nets of extracellular matrix around parvalbumin-containing neurons of the hippocampus. *Hippocampus* 3(Spec No):55–60.

31. Galtrey CM, Fawcett JW (2007) The role of chondroitin sulfate proteoglycans in regeneration and plasticity in the central nervous system. *Brain Res Brain Res Rev* 54(1): 1–18.

32. Bavelier D, Levi DM, Li RW, Dan Y, Hensch TK (2010) Removing brakes on adult brain plasticity: From molecular to behavioral interventions. *J Neurosci* 30(45):14964–14971.

33. Galarreta M, Hestrin S (2001) Electrical synapses between GABA-releasing interneurons. *Nat Rev Neurosci* 2(6):425–433.

34. Bartos M, Vida I, Jonas P (2007) Synaptic mechanisms of synchronized gamma oscillations in inhibitory interneuron networks. *Nat Rev Neurosci* 8(1):45–56.

35. Galarreta M, Hestrin S (2001) Spike transmission and synchrony detection in networks of GABAergic interneurons. *Science* 292(5525):2295–2299.

36. Bartos M, et al. (2002) Fast synaptic inhibition promotes synchronized gamma oscillations in hippocampal interneuron networks. *Proc Natl Acad Sci USA* 99(20): 13222–13227.

37. Doischer D, et al. (2008) Postnatal differentiation of basket cells from slow to fast signaling devices. *J Neurosci* 28(48):12956–12968.

38. Griffen TC, Wang L, Fontanini A, Maffei A (2012) Developmental regulation of spatio-temporal patterns of cortical circuit activation. *Front Cell Neurosci* 6:65.

39. Olivas ND, Quintanar-Zilinskas V, Nenadic Z, Xu X (2012) Laminar circuit organization and response modulation in mouse visual cortex. *Front Neural Circuits* 6:70.

40. Feller MB, Scanziani M (2005) A precritical period for plasticity in visual cortex. *Curr Opin Neurobiol* 15(1):94–100.

41. Fagiolini M, Hensch TK (2000) Inhibitory threshold for critical-period activation in primary visual cortex. *Nature* 404(6774):183–186.

42. Wang BS, Sarnaik R, Cang J (2010) Critical period plasticity matches binocular orientation preference in the visual cortex. *Neuron* 65(2):246–256.

43. Lazarus MS, Krishnan K, Huang ZJ (2013) GAD67 deficiency in parvalbumin interneurons produces deficits in inhibitory transmission and network disinhibition in mouse prefrontal cortex. *Cereb Cortex* 25(5):1290–1296.

44. Simmons DR, et al. (2009) Vision in autism spectrum disorders. *Vision Res* 49(22): 2705–2739.

45. Jones W, Klin A (2013) Attention to eyes is present but in decline in 2-6-month-old infants later diagnosed with autism. *Nature* 504(7480):427–431.

46. Levelt CN, Hübener M (2012) Critical-period plasticity in the visual cortex. *Annu Rev Neurosci* 35:309–330.

47. Chattopadhyaya B, et al. (2007) GAD67-mediated GABA synthesis and signaling regulate inhibitory synaptic innervation in the visual cortex. *Neuron* 54(6):889–903.

48. Donato F, Rompani SB, Caroni P (2013) Parvalbumin-expressing basket-cell network plasticity induced by experience regulates adult learning. *Nature* 504(7479):272–276.

49. Huang ZJ (2009) Activity-dependent development of inhibitory synapses and innervation pattern: Role of GABA signalling and beyond. *J Physiol* 587(Pt 9): 1881–1888.

50. Dupuy ST, Houser CR (1996) Prominent expression of two forms of glutamate decarboxylase in the embryonic and early postnatal rat hippocampal formation. *J Neurosci* 16(21):6919–6932.

51. Jin H, et al. (2003) Demonstration of functional coupling between gamma -amino-butyric acid (GABA) synthesis and vesicular GABA transport into synaptic vesicles. *Proc Natl Acad Sci USA* 100(7):4293–4298.

52. Hsu CC, et al. (2000) Association of L-glutamic acid decarboxylase to the 70-kDa heat shock protein as a potential anchoring mechanism to synaptic vesicles. *J Biol Chem* 275(27):20822–20828.

53. Eggermann E, Jonas P (2012) How the 'slow' Ca(2+) buffer parvalbumin affects transmitter release in nanodomain-coupling regimes. *Nat Neurosci* 15(1):20–22.

54. Tian N, et al. (1999) The role of the synthetic enzyme GAD65 in the control of neuronal gamma-aminobutyric acid release. *Proc Natl Acad Sci USA* 96(22):12911–12916.

55. Pangratz-Fuehrer S, Hestrin S (2011) Synaptogenesis of electrical and GABAergic synapses of fast-spiking inhibitory neurons in the neocortex. *J Neurosci* 31(30): 10767–10775.

56. Bartos M, Alle H, Vida I (2011) Role of microcircuit structure and input integration in hippocampal interneuron recruitment and plasticity. *Neuropharmacology* 60(5): 730–739.

57. Hu H, Gan J, Jonas P (2014) Interneurons. Fast-spiking, parvalbumin+ GABAergic interneurons: From cellular design to microcircuit function. *Science* 345(6196):1255263.

58. Noutel J, Hong YK, Leu B, Kang E, Chen C (2011) Experience-dependent retinogeniculate synapse remodeling is abnormal in MeCP2-deficient mice. *Neuron* 70(1): 35–42.

59. Di Cristo G, et al. (2007) Activity-dependent PSA expression regulates inhibitory maturation and onset of critical period plasticity. *Nat Neurosci* 10(12):1569–1577.

60. He LJ, et al. (2014) Conditional deletion of Mecp2 in parvalbumin-expressing GABAergic cells results in the absence of critical period plasticity. *Nat Commun* 5:5036.

61. Wang BS, Feng L, Liu M, Liu X, Cang J (2013) Environmental enrichment rescues binocular matching of orientation preference in mice that have a precocious critical period. *Neuron* 80(1):198–209.

62. Tropea D, et al. (2009) Partial reversal of Rett syndrome-like symptoms in MeCP2 mutant mice. *Proc Natl Acad Sci USA* 106(6):2029–2034.

63. Djukic A, Rose SA, Jankowski JJ, Feldman JF (2014) Rett syndrome: Recognition of facial expression and its relation to scanning patterns. *Pediatr Neurol* 51(5):650–656.

64. Lewis TL, Maurer D (2005) Multiple sensitive periods in human visual development: Evidence from visually deprived children. *Dev Psychobiol* 46(3):163–183.

65. Toyoizumi T, et al. (2013) A theory of the transition to critical period plasticity: Inhibition selectively suppresses spontaneous activity. *Neuron* 80(1):51–63.

66. He M, et al. (2012) Cell-type-based analysis of microRNA profiles in the mouse brain. *Neuron* 73(1):35–48.

67. Tamamaki N, et al. (2003) Green fluorescent protein expression and colocalization with calretinin, parvalbumin, and somatostatin in the GAD67-GFP knock-in mouse. *J Comp Neurol* 467(1):60–79.

68. Esclapez M, Tillakaratne NJ, Kaufman DL, Tobin AJ, Houser CR (1994) Comparative localization of two forms of glutamic acid decarboxylase and their mRNAs in rat brain supports the concept of functional differences between the forms. *J Neurosci* 14(3 Pt 2):1834–1855.

69. Wang L, Fontanini A, Maffei A (2011) Visual experience modulates spatio-temporal dynamics of circuit activation. *Front Cell Neurosci* 5:12.

70. Niell CM, Stryker MP (2008) Highly selective receptive fields in mouse visual cortex. *J Neurosci* 28(30):7520–7536.

71. Brainard DH (1997) The Psychophysics Toolbox. *Spat Vis* 10(4):433–436.

72. Pelli DG (1997) The VideoToolbox software for visual psychophysics: Transforming numbers into movies. *Spat Vis* 10(4):437–442.

73. Cang J, Kalatsky VA, Löwel S, Stryker MP (2005) Optical imaging of the intrinsic signal as a measure of cortical plasticity in the mouse. *Vis Neurosci* 22(5):685–691.

74. Sato M, Stryker MP (2008) Distinctive features of adult ocular dominance plasticity. *J Neurosci* 28(41):10278–10286.

75. Kalatsky VA, Stryker MP (2003) New paradigm for optical imaging: Temporally encoded maps of intrinsic signal. *Neuron* 38(4):529–545.

76. Katz DM, et al. (2012) Preclinical research in Rett syndrome: Setting the foundation for translational success. *Dis Model Mech* 5(6):733–745.

77. Belichenko PV, et al. (2009) Widespread changes in dendritic and axonal morphology in Mecp2-mutant mouse models of Rett syndrome: Evidence for disruption of neuronal networks. *J Comp Neurol* 514(3):240–258.